Arch. Min. Sci. **71** (2026), 2, 303-335

Electronic version (in color) of this paper is available: http://mining.archives.pl

DOI: https://doi.org/10.24425/ams.2026.158819

JINZHENG BAI[1,2,3,4*], XIUFENG ZHANG[1,3], LINMING DOU[4], SIYUAN GONG[4], ANYE CAO[4], LEIGANG MIAO[2], HONGJUN GUO[2], CUNWEN WANG[1,3], CHUANCHENG LIU[1,3]

MINING INTENSITY EFFECT OF COAL BURST INDUCED BY ULTRA-THICK COMPOSITE KEY STRATUM MOVEMENT: AN EXPERIMENTAL STUDY

Increasing mining intensity complicates overlying strata movement and elevates coal burst risk. However, the mechanism of coal burst initiation under the coupled response of displacement, stress, and vibration fields remains poorly understood. This study investigates a coal burst-prone mine in Northwest China characterised by compound key strata. Through laboratory experiments and theoretical analysis, the development of transverse and longitudinal fractures in the overburden induced by mining was examined. The mechanical mechanism of coal burst under varying mining intensities was revealed based on the response of the stress and vibration fields in the overburden. Results show that as mining intensity increases, overburden activity becomes more incomplete and the energy released by fracturing rises sharply. The voussoir beam structure at lower levels transforms into a high-level cantilever beam. Within the same advancing range, higher mining intensity reduces the frequency of roof weighting but increases the weighting interval and ultimate suspended roof length. The fracture range progressively extends upward. In terms of stress response magnitude and timing, the order is: high-level key stratum < mid-level key stratum < low-level key stratum. During low-speed mining, vibration signals are continuous, low-energy, and high-frequency, indicating progressive overburden failure. In contrast, rapid mining produces sudden, high-energy, and low-frequency signals, associated with large-scale roof suspension or sudden key stratum fracture. This study concludes that high-intensity mining intensifies both the degree and scope of overburden movement, significantly elevating static stress and dynamic fracturing loads. When these exceed a critical threshold, an overburden-type coal bursts are readily induced.

Keyword: Mining intensity; Compound key stratum; Mechanical mechanism; Movement of overburden; Static-dynamic load superposition

1 KEY LABORATORY OF COAL MINE ROCK BURST PREVENTION & CONTROL TECHNOLOGY AND EQUIPMENT, NATIONAL MINE SAFETY ADMINISTRATION, CHINA
2 JIANGSU VOCATIONAL INSTITUTE OF ARCHITECTURAL TECHNOLOGY, CHINA
3 SHANDONG ENERGY GROUP CO., LTD., CHINA
4 SCHOOL OF MINES, CHINA UNIVERSITY OF MINING AND TECHNOLOGY, CHINA

* Corresponding author: baijinzheng@cumt.edu.cn

1. Introduction

The Huji'er Te Mining Area in Inner Mongolia is a newly developed large-scale coal deposit in northwestern China. With continuous improvements in the manufacturing level of working face equipment and management capabilities, the intensity of coal resource extraction has been steadily increasing [1-3]. As researchers' understanding and knowledge of high-intensity mining continue to deepen, its definition and connotations have become more comprehensive, encompassing aspects such as mining method, mining speed, face dimensions, weighting intensity, and mining technology. Considering the current mining technology and equipment level, the characteristic indicators of high-intensity stopes mainly include: the working face length generally reaches 300-360 m, and even exceeds 400 m; the advance distance is 3000-5000 m; the maximum single mining height reaches 8.8 m; and the mining speed can be as high as 20 m/d [4,5]. During the extraction process in high-intensity mining panels, the movement laws of overburden become more complex. Dynamic disasters such as large-scale roof cutting and support failure, significant dynamic pressure impacts on supports, instantaneous outbursts of local coal and rock masses, and extensive failure of coal walls are occurring with increasing frequency. Consequently, the movement characteristics of overburden under high-intensity mining and the mechanical mechanisms triggering rock bursts are attracting growing attention.

Numerous studies have focused on the overburden structure and mining-induced stress field under high-intensity mining conditions [6]. Wang et al. [7] suggested that increasing the working face advance rate is equivalent to increasing the loading rate of the main roof cantilever beam, leading to an increase in both the ultimate tensile strain and the ultimate span of the main roof, thereby intensifying the dynamic loading impact effect. Yang et al. [8] argued that coal and rock are rate-dependent materials. As the loading rate increases, the failure mode of compressed coal and rock transitions from static to dynamic failure. Both the maximum principal stress loading rate and the minimum principal stress unloading rate in the coal ahead of the coal wall increase, raising the strain energy density in the coal mass and consequently increasing the probability and severity of dynamic failure in the surrounding rock. Feng et al. [9], through theoretical analysis, explained the influence of mining speed on the abutment pressure and energy released by roof failure in the mining face, simulated the spatiotemporal evolution characteristics of mine tremor energy in surrounding rock during mining, and statistically analysed the effect of mining speed on the energy and frequency distribution of mine tremors. Yang et al. [10] developed a two-dimensional energy dissipation theoretical model based on the law of energy conservation, established an evaluation index system for fracture damage in overburden, and quantitatively analysed the scale effects of mining parameters using damage indicators, thereby evaluating the effectiveness of optimised mining parameters in reducing damage. Zhang et al. [11], using finite element and discrete element simulation methods, derived quantitative relationships between overburden damage and working face length and advance rate, enabling rational optimisation of mining parameters. Liu et al. [12] revealed the failure types, failure relationships, and development characteristics of water-conducting fracture zones in overburden in western high-intensity mining areas. By considering key factors such as mining thickness and bedrock thickness, they proposed a predictive formula for calculating the height of water-conducting fracture zones under high-intensity mining. Li et al. [13], through analysis of microseismic monitoring data from typical high-intensity mining mines, concluded that as mining speed increases, the number of mining-induced microseismic events and the area of stress redistribution decrease, the uniformity of stress redistribution deteriorates further, and energy release becomes unstable, potentially triggering dynamic failure. Guo et al. [14] proposed critical suspended and spanning distances for determining the failure of various rock strata, established mechanical models for the suspension integrity and caving stability of rock layers, and introduced a theoretical method for predicting the height of fracture zones in high-intensity longwall mining faces. Feng et al. [15], based on elastic mechanics theory and numerical simulations, investigated the influence mechanism of mining intensity on energy release in mining faces. Their conclusions indicated that higher mining speeds result in larger periodic fracture scales of low-position sub-key strata, generating greater static and dynamic loads from bending subsidence and inputting more energy into the coal mass, thereby increasing the likelihood of inducing rock bursts.

Regarding the influence mechanism of mining intensity on coal burst, Xie et al. [16] showed that increasing the advance rate of a fully mechanised top coal caving face would raise the peak value of the advance abutment pressure and shift it closer to the coal wall. Wang et al. [17] suggested that the mining speed affects the stress transfer process in surrounding rock, the loading-unloading rate of surrounding rock, and the creep effect of rock to varying degrees, and appropriately increasing the advance rate of fully mechanised caving faces is conducive to face management and safe production. Wang et al. [18] argued that differences in strata pressure resulting from different mining speeds are mainly reflected in the time-dependent effects of deformation and failure of the surrounding rock. Zhao et al. [19] studied the relationship between the mining speed of the working face and the bending deformation energy of the roof, concluding that as the mining speed increases, the energy released by the roof shows an exponential growth trend. Zhang et al. [20] used laboratory tests, numerical simulations, and field microseismic monitoring to propose an optimised layout and safe advance rate for isolated working faces under hard strata conditions. Liu et al. [21], through case studies and microseismic statistical analysis, concluded that high-speed mining and non-uniform advance rates are prone to inducing coal bursts. Pan et al. [22] explicitly stated that the safe advance rate of mining and excavation faces should be determined based on coal burst risk assessment results. Tang et al. [23] studied the influence of mining rate on mine microseismic activity and introduced the concept of response coefficient (CSR) using quantitative seismology methods to characterise the relationship between energy storage and release in rock masses, providing guidance for field production. Yang et al. [24] found that the faster the working face advance rate, the greater the loading rate of overburden on the main roof. When the loading rate is high, the failure time of coal samples is shorter, and the sound emitted during failure is louder. Li et al. [25] argued that the dynamic load disturbance from mine tremors caused by overburden movement in fully mechanised caving mining is one of the important factors inducing coal burst and provided a basis for determining the reasonable pre-splitting roof cutting distance.

Guo et al. [26] defined high-intensity mining as a high-yield and efficient coal mining method characterised by thick coal seams, full-seam mining with fully mechanised mining, large working face dimensions, rapid advance rates, and high single-face output. Further, by analysing the influence of mining thickness, dimensions, and depth on the full mining-induced failure of overburden, they proposed a criterion formula for determining full mining-induced failure under high-intensity mining and provided corresponding parameter indicators. Tan et al. [27] identified high advance rates, high width-to-depth ratios, and high extraction rates as characteristic features of high-intensity mining in mines. Fan et al. [28] considered high-intensity mining to be characterised by large working face dimensions and rapid advance rates. Xu et al.

[29] argued that the intrinsic reason for the frequent occurrence of roof disasters is the increase in caving zone height caused by the multiplied increase in mining height and working face length in high-intensity mining faces, which subsequently leads to changes in the mechanical model of roof control. Guo et al. [30] regarded high-intensity mining as a mining method that induces intense movement in overburden or surface subsidence, and proposed corresponding evaluation indicators based on surface subsidence velocity, fracture zone width, and dynamic load coefficient of the mining face.

However, few studies have systematically investigated the transition of overburden structure under different mining intensities, nor have they revealed the multi-field coupled response mechanisms. This study first investigates the fine development process of transverse and longitudinal fractures in overburden induced by mining through physically similar material simulation experiments, followed by a comparative analysis of the response mechanisms of overburden stress fields and vibration fields under different mining intensities. Building on this, a mechanical mechanism of coal burst influenced by mining intensity effects is proposed, which can subsequently provide guidance for determining appropriate mining intensity in coal-burst-prone mines.

2. Experimental design

2.1. Study area

The Shilawusu Coal Mine studied in this similarity experiment is affiliated with Shandong Energy Group, located in the northeastern part of the Hujierte Mining Area within the Dongsheng Coalfield in China. The mine has a designed production capacity of 8.00 Mt/a. The primary mining seam is the 2-2 coal seam, situated in the Middle-Lower Jurassic Yan'an Formation, with an average burial depth of 660 m and an average thickness of 4.5 m. Both the coal seam and its roof and floor exhibit weak bursting tendencies, while the 2-2 coal seam is classified as having moderate bursting risk. Since 2021, the Shilawusu Coal Mine has experienced five strong mine seismic events with a Richter magnitude scale exceeding 2.0 (2.3E+07 J), among which three typical ultrathick overburden-type strong mine seismic events occurred during the mining of Panel 1208, as shown in TABLE 1.

Although the occurrence of mine tremors did not cause damage to underground roadways, ground vibrations were perceptible in all cases. As a result, the mine was forced to suspend production for a cumulative total of over 290 days, severely affecting mine sequencing planning as well as safe and efficient production. The mine exhibits complex geological conditions, including great depth, high stress, thin bedrock, and thick, hard roof strata. The stratigraphic characteristics of the composite key layers are shown in Fig. 1. Borehole information consistently indicates the presence of high-position Lower Cretaceous Zhidan Group strata, mid-position Middle Jurassic Zhiluo Formation strata, and low-position Lower Jurassic Yan'an Formation strata. The interaction among multiple key layers results in a pronounced composite key layer effect, which enhances the overall integrity of strata movement and load-bearing capacity, leading to a higher stress concentration factor and increased risk of coal burst.

To further clarify the correlation between mining intensity and coal burst risk, historical data on total microseismic energy and event frequency under different daily advance rates at Panel 1208 were selected for statistical analysis. As shown in Fig. 2, a significant correlation exists

TABLE 1

Occurrence of strong mine tremors in Panel 1208 under adjacent goaf mining conditions

Date	Location description	Energy/J	Magni-tude	Distance to the lagging working face/m	On-site conditions
2021/08/20	Panel 1208 advanced to a position 289.9 m from the starting face of Panel 1206A, with the event occurring within the goaf of Panel 1208.	5.56E+05	2.40	218	No noticeable tremor was felt underground, with no observable changes in the roadway; a slight tremor was sensed on the surface of the industrial area, and all ground structures and facilities remained unaffected.
2021/08/29	During the blasting operations in the suspended production period of Panel 1208, the event occurred within the goaf of Panel 1208.	1.69E+05	2.80	264	No noticeable tremor was felt underground, with no observable changes in the roadway; a slight tremor was sensed on the surface of the industrial area, and all ground structures and facilities remained unaffected.
2021/12/20	When Panel 1208 advanced to a position 398.2 m from the starting face of Panel 1206A, the event occurred within the goaf of Panel 1206A.	2.92E+05	2.60	72	No noticeable tremor sensation was observed underground, with no significant changes in the roadways or monitoring systems; a slight tremor sensation was felt on the surface, but no damage occurred to surface structures and buildings, and no casualties or property losses were reported.

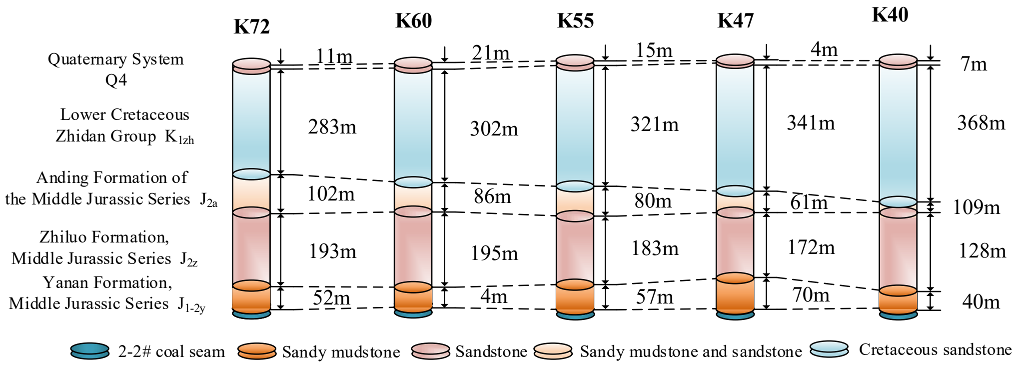

Fig. 1. Stratigraphic characteristics of the key strata in the Shilawusu Coal Mine

between the daily advance rate of the working face and microseismic temporal indicators, with a clear inflexion point observed within the range of advance rate variation. This indicates that under the influence of mining intensity effects, the adjustment characteristics of the composite thick-hard overburden strata differ, thereby altering the coal burst risk in the mining area. Therefore, employing research methods to reveal the movement patterns of composite key strata under different mining intensities is of great significance for reasonably determining the safe mining intensity of the working face.

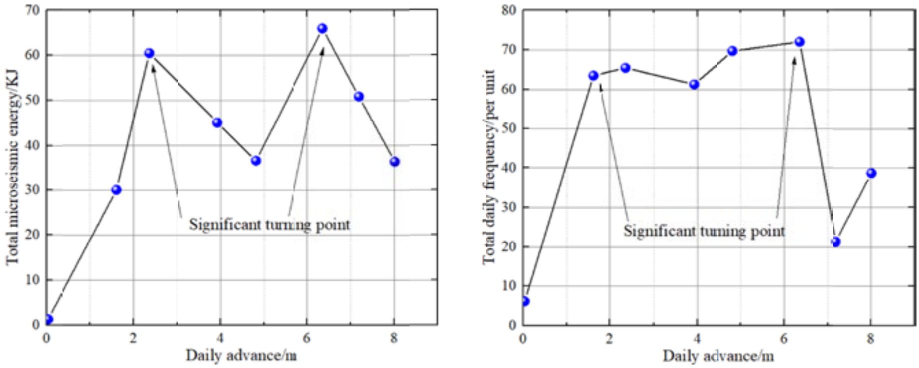

(a) daily advance rate – Total energy (b) daily advance rate – Total frequency

Fig. 2. Correlation between mining intensity and microseismic temporal indicators in Shilawusu Coal Mine

2.2. Model design

Based on the aforementioned rock mass stratigraphy in the Shilawusu Coal Mine, with a combination of geological borehole logs drilling next to the 1208 mining panel, the distribution of the roof strata next to the 2-2 coal seam was reasonably simplified to establish a physical similarity model of the key stratum. The experimental equipment is located at the National Key Laboratory for Fine Exploration and Intelligent Development of Coal Resources at CUMT. The dimensions of the similarity simulation test platform were determined as length × height × thickness = 2500 mm × 1600 mm × 300 mm, with a geometric similarity ratio of α = 1:400. The simulated area includes Panel 1208, with a strike mining length of 800 m. The mining process was divided into five stages according to different pre-mining conditions, each with a strike length of 160 m. On both sides, 40 m-wide (in scale 1:400) non-excavation zones were reserved to simulate boundary coal pillars, reducing the influence of the test platform boundaries, as shown in Fig. 3. In this

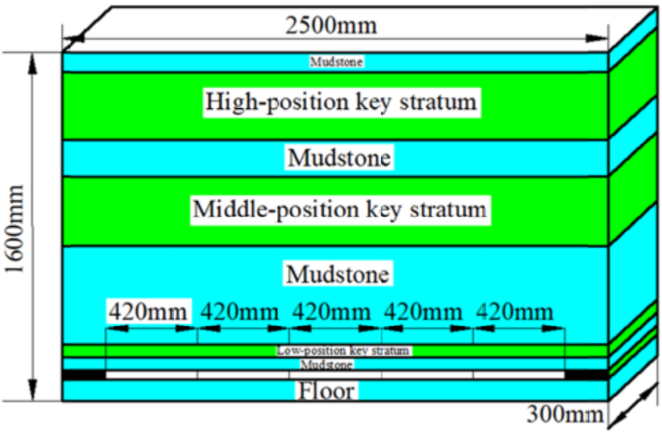

Fig. 3. Schematic of the model simulation

simulation, the burial depth of the 2-2 coal seam is approximately 660 m, with a simulated coal seam thickness of 16 m. A 40 m-thick floor stratum was set at the bottom, and 584 m of roof strata were laid above. The average dip angle of the coal seam in the simulated area is about 7°, while the coal and rock strata were laid horizontally. The overlying load from the 400 m-thick rock layers above the model was compensated by applying an external load via an airbag, with an equivalent applied load of 16 kPa.

2.3. Model similarity ratio and similar materials

The similarity conditions in a physically similar material model can be defined as the proportional relationships between the geometric features and physical quantities of the model and the prototype. Based on similarity theory, the similarity ratios for stress, displacement, strength, and time in this similar material model are shown in TABLE 2.

TABLE 2

Model similarity ratio

Parameters	Geometry	Bulk density	Stress	Displacement	Strength	Time	Dimensionless quantity
Similarity ratio	1:400	1:1.5	1:600	1:400	1:600	1:20	1:1

Based on the material selection principles for similar material simulation models, this experiment uses fine river sand as the aggregate, calcium carbonate and gypsum as the cementing agents, water as the binder, and mica powder as the interlayer interface material. The mix ratio of the similar materials is primarily determined according to the bulk density and strength parameters of the coal and rock strata. After repeated adjustments, the optimal mix ratio for each layer of similar material was finalised. Then, based on the cross-sectional area of the model frame, the simulated thickness of the coal and rock layers, and the geometric similarity ratio, the required volume of each similar material was calculated. Subsequently, the weight of similar materials for each coal and rock layer was derived from the density and mix ratio of the materials. The final mix proportions for this experiment are shown in TABLE 3.

TABLE 3

Model material formulation

No.	Strata	Thickness /m	Layer thickness /cm	Mix proportion designation	Total dry weight /kg	Fine river sand /kg	Lime /kg	Gypsum /kg
1	Mudstone	36	9	673	114.75	98.36	11.48	4.92
2	Sandstone	124	31	473	395.25	316.20	55.34	23.72
3	Mudstone	68	17	673	216.75	185.79	21.68	9.29
4	Sandstone	128	32	473	408.00	326.40	57.12	24.48
5	Mudstone	180	45	673	573.75	491.79	57.38	24.59
6	Sandstone	24	6	473	76.50	61.20	10.71	4.59
7	Mudstone	24	6	673	76.50	65.57	7.65	3.28
8	2-2 coal	16	4	773	51.00	44.63	4.46	1.91
9	Mudstone	16	4	673	51.00	43.71	5.10	2.19
10	Mudstone	24	6	673	76.50	65.57	7.65	3.28

According to the aforementioned proportion and material quantity of each rock stratum, the dry materials of each layer were sequentially mixed uniformly, followed by water addition and stirring, before being loaded into the model, levelled, and tamped to the designed thickness. To better observe the development and fracturing of cracks in the rock strata, a thin layer of white latex paint was applied to the surface of the model after completion, and a coal seam position was painted in black. The prepared model and its initial loading conditions are shown in Figs. 4 and 5.

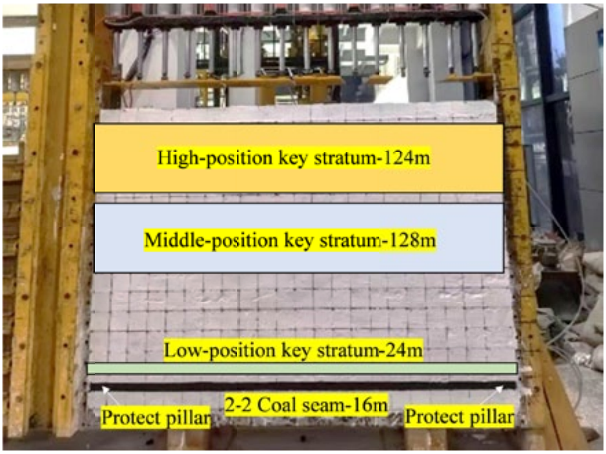

Fig. 4. Initial state of the model

Fig. 5. Initial loading of the model

2.4. Experiment plan and monitoring equipment

After the model was completed, it was left to cure for one week. The experience in physical model building with the use of equivalent materials shows that one week is enough to complete the binding. Subsequently, the channel steel formwork at the front and rear sides was removed in stages. Once the model had dried and reached the designed strength, experimental simulated excavation commenced. The large-scale excavation in the model was carried out sequentially from right to left.

The actual average advance rate of the working face at Shilawusu Coal Mine is approximately 4 m/d. Under the three-shift working system, an advance rate that is an even multiple of the cutting interval of the shearer drum picks is more favourable for coordinating mining activities. Accordingly, five advance rates were designed for the experiment: 2.0, 4.0, 6.0, 8.0, and 10.0 m/d, corresponding respectively to extremely slow, slow, moderate, relatively fast, and high-speed mining conditions.

In a similar simulation experiment, a direct manual excavation method was employed to simulate coal seam mining, with screwdrivers and saw blades as the primary tools. The specific operational steps are as follows: First, the excavation range corresponding to different mining intensities was determined according to the experimental design, and the boundaries were clearly marked on the model surface with a marker pen. Next, a screwdriver was used to carefully create a small-scale opening within the marked area. During this process, the force applied was strictly controlled to ensure that the integrity of the roof and floor remained undisturbed. Finally, a saw blade was used to perform step-by-step excavation along the opening, with the excavation time for each step precisely controlled to simulate the working conditions under different mining intensities.

Actual Excavation Scheme of the Model: To eliminate boundary effects, 10 cm coal pillars were reserved at both ends of the model. An open-off cut was made 10 cm from the right boundary of the model. The coal seam mining area covered the model section from 10 cm to 210 cm, so 200 cm. To exclude the influence of the working face advance length on experimental results, the area to be mined was evenly divided into five stages, corresponding to five mining intensities. Each stage was mined for 40 cm. During the experiment, since the current working face advance rate was temporarily set at 4 m/d, the advance rate in the first stage was designed as 2.0 m/d (0.5 cm per excavation cycle). The subsequent four stages corresponded to 4.0 m/d, 6.0 m/d, 8.0 m/d, and 10.0 m/d, respectively. The experiment was strictly conducted according to the similarity relations and similarity criteria. The mining schemes for working faces under different mining intensities are shown in TABLE 4.

TABLE 4

Model excavation scheme

Mining stage	**Stage I**	**Stage II**	**Stage III**	**Stage IV**	**Stage V**
Model range/cm	10-50	50-90	90-130	130-170	170-210
Mining speed/$m \cdot d^{-1}$	2.0	4.0	6.0	8.0	10.0
Advance speed/1 cm per advance step	0.5	1.0	1.5	2.0	2.5
Number of excavation cycles	80	40	25	20	15

The integrated monitoring system used in this test is shown in Fig. 6(a). According to the test plan, a ZC40YL programmable static resistance strain gauge data acquisition system was employed together with DF-9-2 kg thin-film single-point pressure sensors to monitor the abutment pressure of the surrounding rock during the mining process of the physical similarity model under different mining intensities. These sensors have a thickness of only 0.1-0.2 mm, providing good flexibility. The sensor diameter is 10 mm, with a sensitive area of 7.5 mm. They are capable of converting the pressure applied to the sensitive area into resistance signals, and then, based on the calibrated force-resistance relationship, the variation of the externally applied pressure can be obtained. The greater the pressure, the smaller the resistance output by the sensor. The ZC40YL programmable static resistance strain gauge is shown in Fig. 6(b).

Vibration signals during the mining process were monitored using a PCI-2 Acoustic Emission (AE) Monitoring System and an SOS Microseismic Monitoring System, as shown in Fig. 6(c) and Fig. 6(d). The PCI-2 AE system is a product of Physical Acoustics Corporation (PAC) in the United States. Data acquisition, replay, and post-processing can be performed via its AE Win software. The SOS Microseismic Monitoring System is a new-generation microseismic monitoring instrument designed and manufactured by the Mining Seismology Division of the Polish Central Mining Institute. Featuring simple structure, convenient operation, and high reliability, it has been installed in most mines in Poland and China for monitoring and forecasting coal burst hazards. The SOS system employs vibration-velocity type mine tremor sensors with a frequency range of 0.1 Hz to 600 Hz and embedded signal transmission modules, and uses an independent trunk-line

(a) Overall schematic of the monitoring system

(b) Stress monitoring system

(c) AE monitoring system

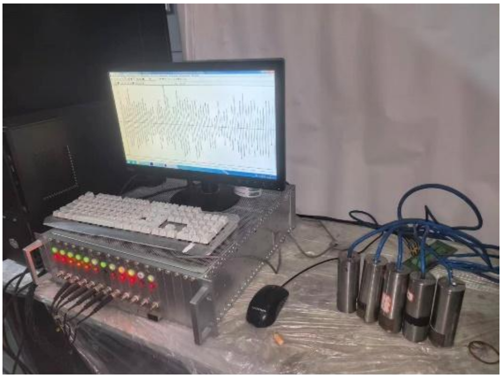
(d) Seismic monitoring system

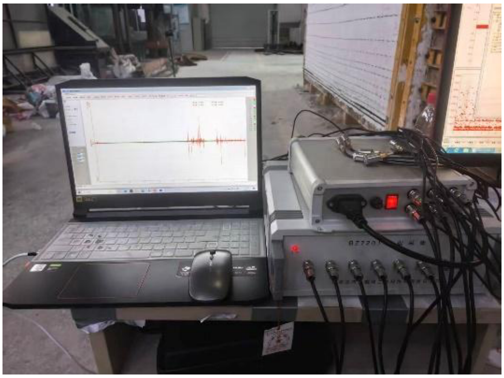
(e) Acceleration monitoring system

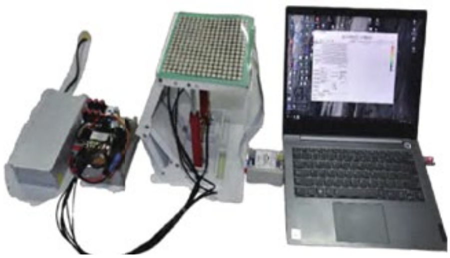
(f) Support load monitoring system


(g) 3D photogrammetric system

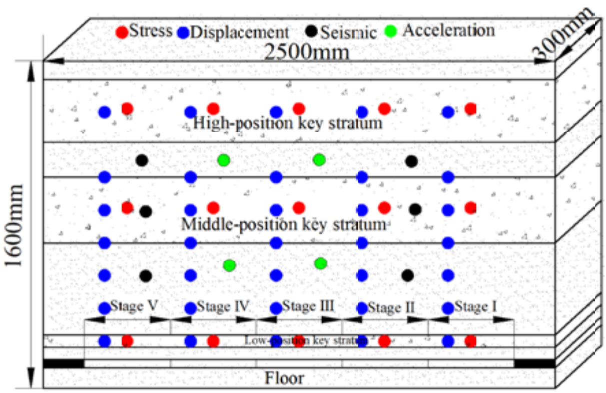

(h) Sensor layout diagram

Fig. 6. Experimental monitoring system

data transmission system for bidirectional control and data transfer. As a regional monitoring method, it offers wide coverage, enabling comprehensive, multi-level continuous monitoring across the entire mine field with high positioning accuracy and small errors. The horizontal positioning error is less than 20 m, the vertical error is less than 50 m, and the monitored energy threshold is ≥100 J. As shown in Fig. 6(e), a BZ7201 high-precision data acquisition instrument produced by Qinhuangdao Beidaihe Land Technology Co., Ltd. was used to monitor acceleration signals generated by overburden movement. This instrument offers advantages such as ease of use, high measurement accuracy, low noise, and massive storage capacity. As shown in Fig. 6(f), a self-developed oil-controlled hydraulic support model was employed to support the roof, with an initial setting load of 100 N, in order to study the influence of overburden movement on support response characteristics under high-intensity mining conditions. The model support consists of a canopy, base, four-bar linkage, hydraulic legs, shield beam, face guard, PLC control unit, control valves, and hydraulic circuits. The Digi-Metric 3D photogrammetric system was used to monitor model deformation during the test (Fig. 6g). Black-background white-center marker points spaced at 100 mm × 100 mm were pasted on the model surface for this purpose, and fixed reference points were installed on the surrounding metal frame. The schematic diagram of the main monitoring system sensor layout adopted by the model is shown in Fig. 6(h).

3. Experimental results

3.1. Response characteristics of the displacement field

The movement and failure characteristics of the overburden under different mining intensities are shown in Figs. 7(a)-7(e). It can be observed that the roof caving exhibits a distinct asymmetric cantilever-hinged structure. As the mining intensity increases, the cantilever length

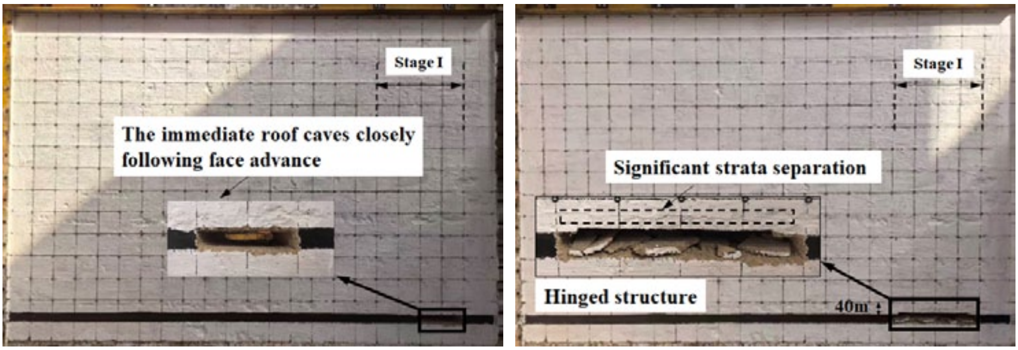

(a) Stage I

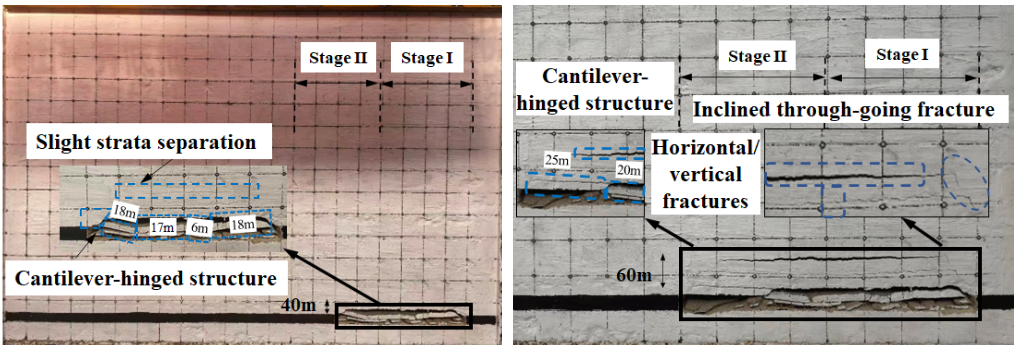

(b) Stage II

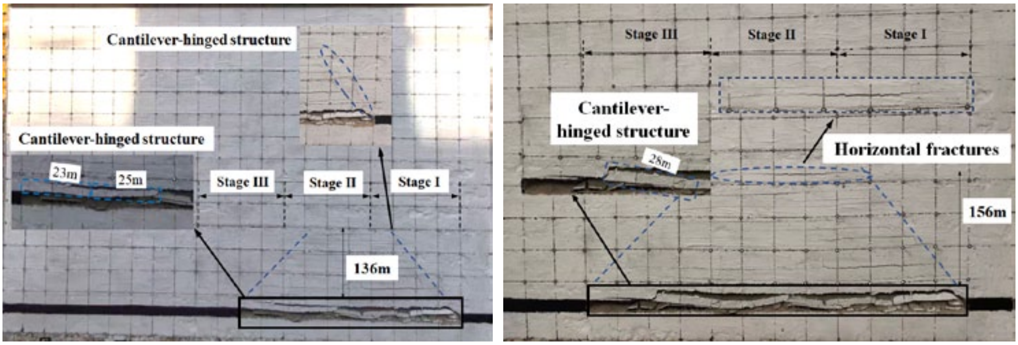

(c) Stage III

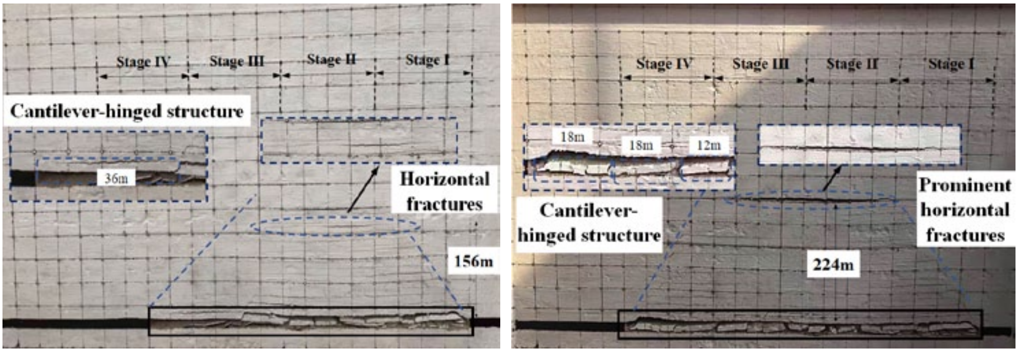

(d) Stage IV

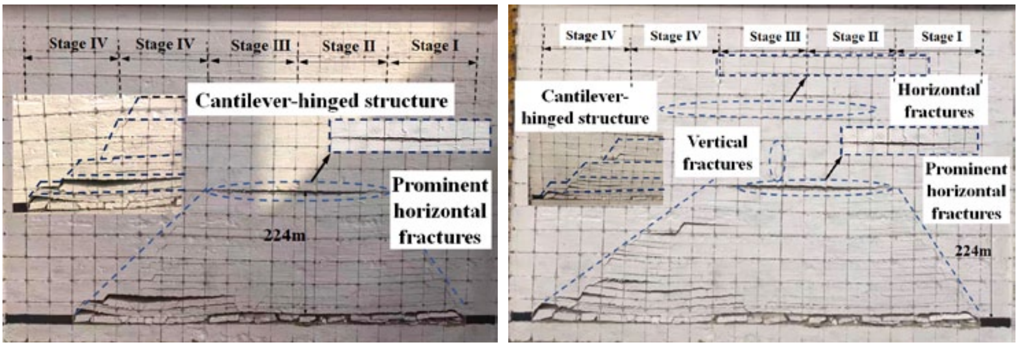

(e) Stage V

Fig. 7. Movement characteristics of overburden

gradually extends, the activity of the overburden becomes increasingly insufficient, and the energy released by fracture rises substantially. This transforms the original low-position fractured voussoir beam structure, which had not yet contacted the goaf debris, into a high-position cantilever beam structure.

As shown in Fig. 7(a), under extremely slow excavation conditions, corresponding to a field advance rate of 2 m/d, the immediate roof caves closely following the face advance. Bed separation between rock layers is relatively evident, rock blocks are relatively fragmented, and the maximum failure height of the overburden reaches about 40 m.

As shown in Fig. 7(b), under slow excavation conditions, corresponding to a field advance rate of 4 m/d, the immediate roof caves closely following face advance. The rock blocks on the left side collapse and stabilise, while the middle rock block remains suspended, bridging over the left-side blocks and forming a cantilever-hinged structure. The cantilever length gradually increases from 18-20 m to 20-25 m, and the maximum failure height of the overburden rises to about 40 m, reaching the level of the low-position key stratum.

As shown in Fig. 7(c), when the mining speed is further increased to moderate mining conditions, corresponding to a field advance rate of 6 m/d, the cantilever length gradually extends to 25-28 m, and the maximum failure height of the overburden rapidly increases to about 136-156 m, approaching the level of the mid-position key stratum.

Subsequently, as shown in Fig.7(d), when the mining speed is increased to fast mining conditions, corresponding to a field advance rate of 8 m/d, the cantilever length continues to increase to about 36 m, and the maximum failure height of the overburden rapidly rises to about 224 m, with step-like subsidence initially observed.

Finally, as shown in Fig 7(e), when the mining speed is increased to extremely fast mining conditions, corresponding to a field advance rate of 10 m/d, horizontal fractures develop in the high-position strata, and the failure level approaches the high-position key stratum. The rock blocks exhibit relatively high integrity and fail to collapse promptly and fully to form a stable structure. Pronounced step-like subsidence occurs above the overburden, accompanied by clearly developed bed-separation cracks. The failure height reaches the level of the high-position key stratum, indicating relatively intense strata failure. TABLE 5 presents the development heights of the overburdened “two zones” under different mining intensities.

TABLE 5

Caved and fractured zone heights under different mining intensities

Mining intensity	**2.0**	**4.0**	**6.0**	**8.0**	**10.0**
height of the caved zone/m	12	40	55	70	90
height of the fractured zone /m	35	165	240	350	430

Fig. 8 shows the displacement contour maps of the overburden under different mining intensities. It can be observed that under the influence of varying mining intensities, the displacement field of the overburden exhibits an overall asymmetric and non-uniform subsidence pattern, which is significantly affected by the mining intensity effect. As the mining intensity increases, the movement of the overburden demonstrates characteristics of being faster, more extensive, and more intense.

As shown in Fig. 8(a), when the mining intensity is relatively low, the goaf area is small, and the subsidence deformation of the overburden is relatively slow. The movement characteristics of the surrounding rock structure correspond to static and uniform adjustment. Under the action of the top loading, minor deformation occurs on both sides of the model. This is due to the presence of side baffles in the test platform during model construction, which prevented the similar materials in the edge zones from being fully compacted; after the top loading was applied, both sides were further compacted, resulting in slight deformation. As shown in Figs. 8(b)-8(c), as the mining intensity gradually increases, the movement of the overburden becomes more

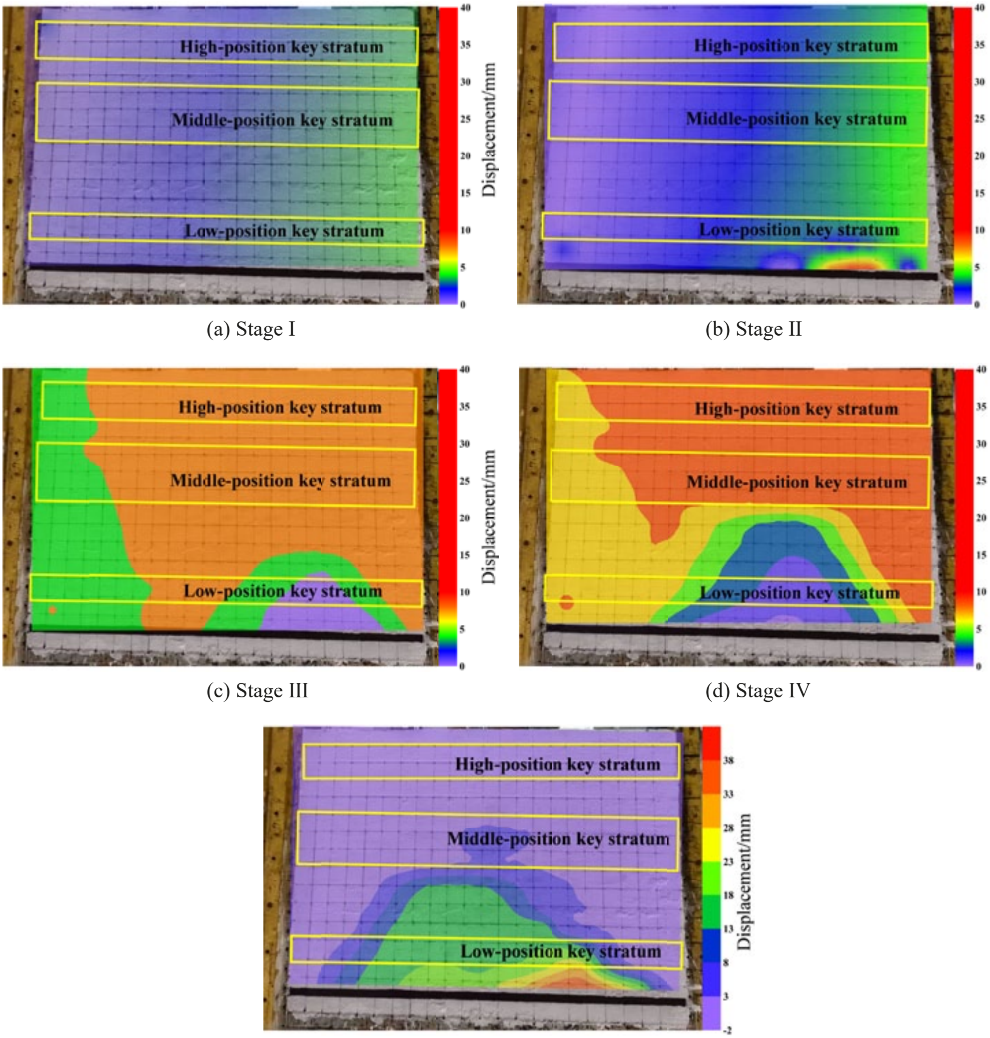

(a) Stage I (b) Stage II

(c) Stage III (d) Stage IV

(e) Stage V

Fig. 8. Displacement contour maps of overburden

pronounced. It begins with the activity of the rock layers below the low-position key stratum, where the suspended roof length is small, and the roof behind the coal wall collapses relatively fully, resulting in a relatively small overall displacement. Subsequently, the low-position key stratum is noticeably affected by mining, exhibiting a certain degree of flexural deformation, and the displacement gradually increases.

As shown in Fig. 8(d), with a further increase in mining intensity, the range of overburden movement rapidly extends upward. The bottom of the mid-position key stratum begins to fail, and the displacement increases significantly, indicating that the overburden fracture follows a layered subsidence pattern at this stage, and the risk of coal burst gradually rises.

Finally, as shown in Fig. 8(e), under ultra-fast excavation conditions, the movement of the overburden becomes even more rapid, the exposed span of the overburden increases, forming a long arc-shaped suspended roof, which ultimately presents a stepped coordinated failure pattern.

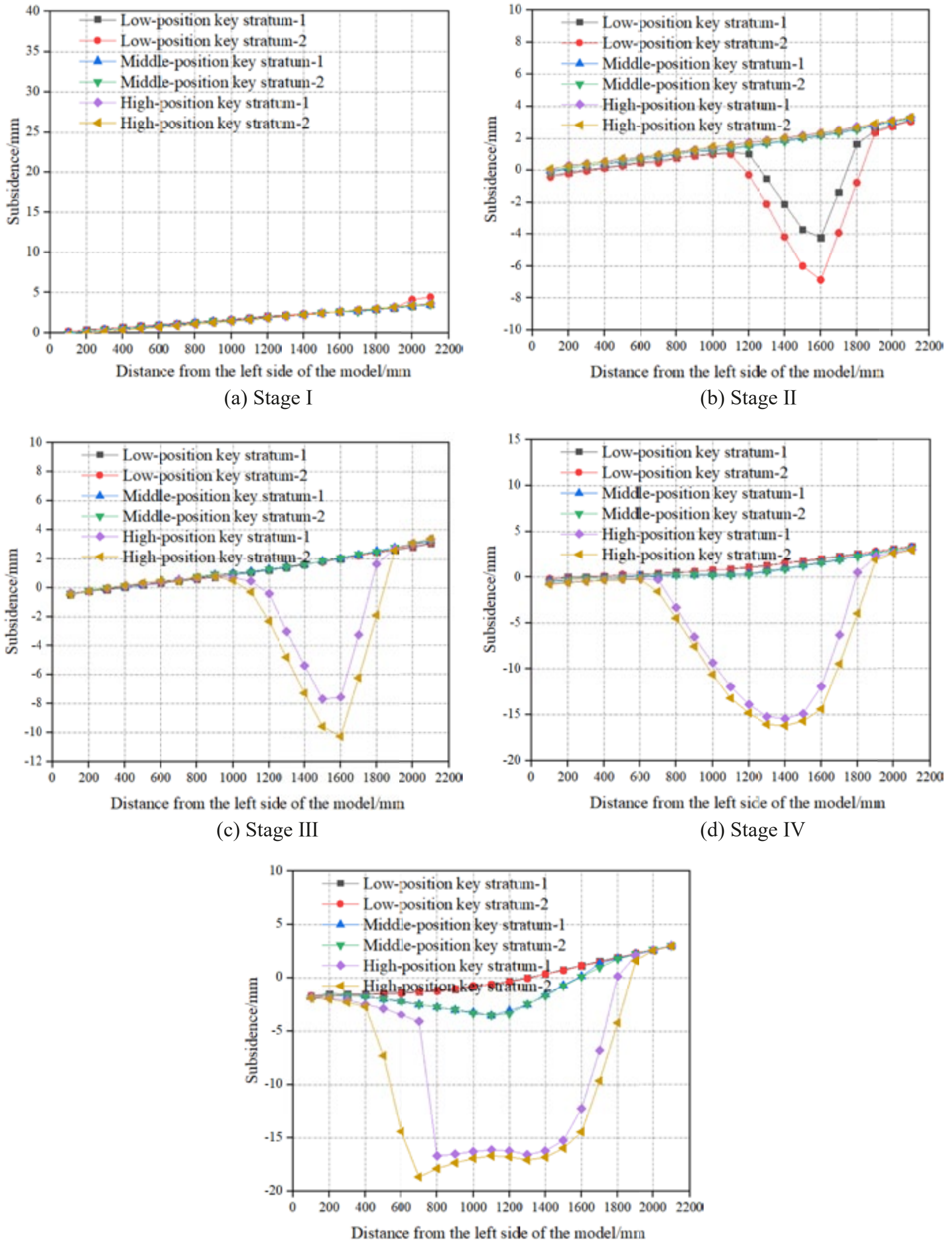

(a) Stage I (b) Stage II

(c) Stage III (d) Stage IV

(e) Stage V

Fig. 9. Displacement variation curves of the overburden

To further quantify and analyse the deformation and movement patterns of the overburden above the goaf, a statistical analysis was conducted on the data from each displacement monitoring point in the model under different mining intensities. Taking the lower-left corner of the model as the zero point, the horizontal axis represents the distance from the left side of the model, and the vertical axis represents the settlement at the measurement point, both in millimetres. The coordinate system is established as shown in Fig. 9.

Fig. 9 presents the displacement variation curves of the measuring lines behind the overburden under different mining intensities. It can be observed that when the mining intensity is relatively low, the subsidence of the overburden is essentially negligible, with even the low-position key stratum not significantly affected by mining. When the mining intensity increases to slow excavation, corresponding to a field advance rate of 4 m/d, the low-position key stratum exhibits marked layered caving, with peak subsidence values of approximately 4 mm and 7 mm, while the mid- and high-position key strata show no obvious settlement.

As the mining intensity rises to moderate excavation, corresponding to a field advance rate of 6 m/d, the mid-position key stratum undergoes significant layered caving, with peak subsidence values of about 8 mm and 10 mm, whereas the high-position key stratum remains largely unaffected.

When the mining intensity further increases to fast excavation, corresponding to a field advance rate of 8 m/d, the mid-position key stratum again shows pronounced layered caving, with peak subsidence values reaching approximately 15 mm and 16 mm, and the high-position key stratum still displays no noticeable settlement.

Finally, under extremely fast excavation, corresponding to a field advance rate of 10 m/d, the mid-position key stratum continues to cave in layers, with peak subsidence values of about 17 mm and 20 mm, while the high-position key stratum again exhibits no significant subsidence.

3.2. Response characteristics of the stress field

Overburden coal burst is fundamentally governed by the distribution and evolution characteristics of the stress field within the coal-rock mass. Compared to other physical parameters, stress serves as the most reliable indicator. In this experiment, support pressure sensors were employed to monitor the weighting intensity at the working face. These sensors were advanced progressively with the face, with a focus on capturing the support pressure data during the fracturing, caving, and weighting of the overburden induced by excavation.

Meanwhile, thin-film pressure sensors were utilised to monitor the evolution of the stress field in the surrounding rock of the goaf during panel extraction. These sensors were installed at specific locations: within the coal seam floor, inside the boundary coal pillars, and in the overlying roof strata above the sandy conglomerate layer.

3.2.1. Periodic weighting pattern of the overburden

During the entire mining process from 20 cm to 220 cm in the model, the overburden experienced a total of 26 weightings, as shown in Fig. 10. Specifically, when the advance rate was 2 m/d, the first large-scale caving of the overlying roof occurred after the working face had advanced by 3 cm, i.e., the initial weighting interval was about 6 cm. Concurrently, the main roof underwent 7 periodic weightings, with an average periodic weighting interval of approximately 4.85 cm, corresponding to 19.4 m in the engineering field. When the mining intensity increased to 4 m/d, the main roof exhibited 6 periodic weightings, with average periodic weighting intervals of about 7.5 cm, 7.5 cm, 8.0 cm, 8.3 cm, and 8.7 cm, respectively, so in the real distance of 30 m, 30 m, 32 m, 33.2 m and 34.8 m.

Within the same advance length range, as the advance rate increased, the number of weightings decreased while the weighting intervals increased accordingly. This led to a larger ultimate suspended span of the overburden, preventing the roof from collapsing fully and promptly within a given time. Consequently, during periodic weightings, the dynamic load disturbance in the stope became more intense, and the potential for instability in the overburden grew accordingly.

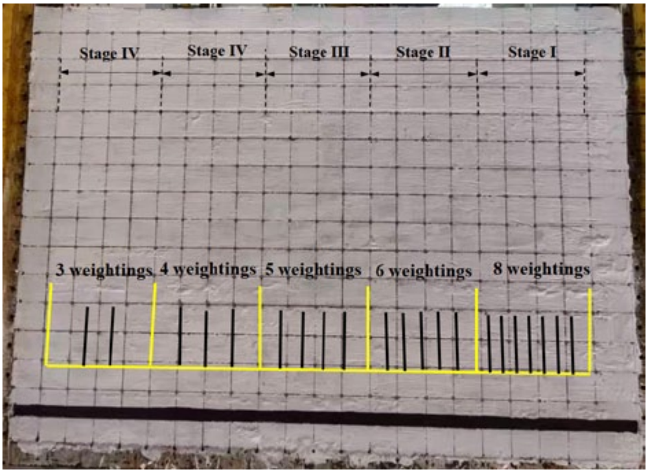

Fig. 10. Weighting conditions of the overburden

As the advance rate increases, within the same mining length, the number of weightings slightly decreases, while the weighting interval and support pressure gradually increase. When the advance rates are 2.0, 4.0, 6.0, 8.0, and 10.0 m/d, the ratios of the weighting interval to the advance rate are 2.5, 1.7, 1.3, 1.3, and 1.25, respectively, showing a clear decreasing trend overall. Meanwhile, the average support pressure progressively rises from 10.0 MPa to 38.4 MPa with increasing mining speed, corresponding to increments of 14.1%, 44.2%, 50.2%, and 18.1%, respectively.

The characteristics of overburden weighting during the mining period are summarised in TABLE 6, and the corresponding weighting conditions are illustrated in Fig. 10.

TABLE 6

Characteristics of strata weighting

Advance rate (m/d)	**2.0**	**4.0**	**6.0**	**8.0**	**10.0**
Number of weightings	8	6	5	4	3
Average periodic weighting interval /m	5.0	6.7	8.0	10.0	13.3
Interval-to-intensity ratio	2.5	1.7	1.33	1.3	1.25
Peak support pressure /MPa	10.04	15.44	21.93	27.36	38.42

3.2.2. Evolution of surrounding rock stress

Due to issues such as uneven placement of sensors during model construction, insufficient tamping of the model material, and water ingress into sensors, some sensors failed to collect valid pressure data. Therefore, a subset of representative monitoring data from high-, mid-, and low-position sensors was selected for detailed analysis. The evolution of stress in the overburden at the positions of the high-, mid-, and low-position key layers under different mining intensities is shown in Fig. 11.

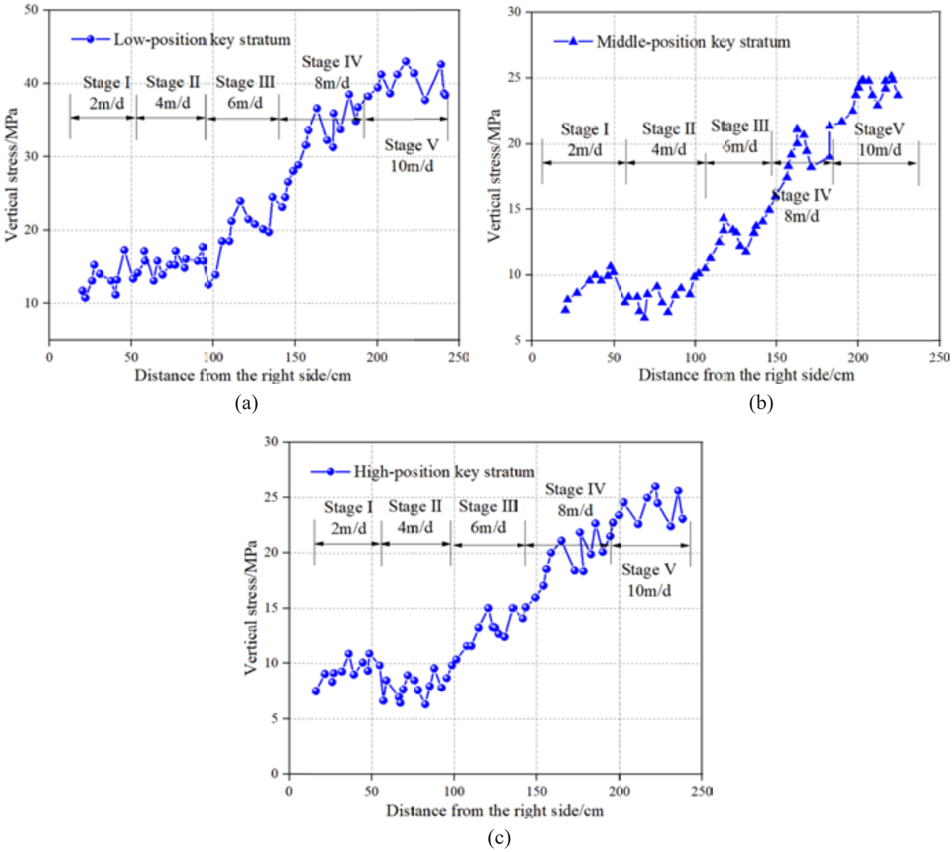

Fig. 11. Evolution of surrounding rock stress

As shown in Fig. 11(a), when the mining intensity is relatively low, the surrounding rock stress near the low-position key stratum responds first, remaining at a relatively low overall level with insignificant fluctuations during excavation, where the vertical stress ranges approximately between 800 kN and 1500 kN. Subsequently, as the mining intensity increases, the surrounding rock stress rises slightly but not substantially, still remaining roughly within the range of 1000 kN to 1500 kN. When the mining intensity continues to increase, the stress in the low-position key stratum area begins to rise significantly and persistently, indicating that the overburden movement has entered a relatively active stage, with fluctuations ranging from about 1000 kN to 2000 kN. Thereafter, when the mining intensity further increases to the fast-mining stage, the stress in the overburden also rises correspondingly to approximately 2000 kN to 3000 kN. Finally, when the mining intensity reaches the extremely fast mining stage, the surrounding rock stress continues to show an upward trend, but the magnitude of increase is markedly reduced, essentially stabilising within the range of 3000 kN to 3500 kN.

As shown in Figs. 11(b)-11(c), compared with the low-position key stratum, the evolution trends of surrounding rock stress in the mid- and high-position key strata are generally consistent, all exhibiting a variation pattern of "low-level fluctuations in the early stage, rapid and sustained growth in the middle stage, and slowed growth rate in the later stage". The differences lie in the following aspects: (1) As the stratum position rises, the surrounding rock stress at the same horizontal location gradually decreases. The stress level in terms of stress level increases from the low-position key stratum, through the mid-position, to the high-position. (2) As the stratum position increases, the response time of surrounding rock stress to mining influence is relatively delayed, and the stress adjustment period progressively lengthens. So, regarding the timing of stress response, the fastest is in the low-position key stratum, then occurs in mid-position rock beds and eventually in high-position stratum. After the overburden rock fractures and collapses, the roof load is first transferred to the coal walls on both sides of the goaf, forming a pressure arch. This leads to an increase in the stress level of the lower key stratum, while the middle and upper overburden continue to function in the form of a "plate" to support the stability of the overburden. As the working face continues to advance, the failure height of the overburden gradually develops upward, and the height and range of the pressure arch continuously increase. When it reaches the middle and upper overburden, localised stress concentration is induced. (3) Under low mining speeds, the influenced zone of the pressure-increase segment is larger, the peak pressure-increase load is lower, and the peak location is farther from the coal wall. Under high-speed mining conditions, due to insufficient stress transfer and adjustment around the stope, the stress concentration coefficient in the surrounding rock is higher. This results in a smaller influenced zone of the pressure-increase segment, a higher peak pressure-increase load, and a peak location closer to the coal wall. Consequently, the elastic core accumulated within the coal mass is closer to the exposed free surface, significantly increasing the likelihood of coal burst occurrence. It is worth noting that vertical pressure rises about 3 times in every key stratum when the longwall panel face advance increases from 2 m/d to 10 m/d. This information can be very important in mining practice, e.g., to assess the possible load on hydraulic support or steel support frames in gates.

3.3. Response characteristics of the seismic field

Coal seam mining disrupts the stability of the original strata structure, leading to a redistribution of the virgin stress field. When the stress exceeds the ultimate strength of the coal-rock mass, instability failure occurs. Among these, static failure manifests as conventional mine pressure, while dynamic failure is expressed as overburden coal burst. The energy released from the coal-rock mass generates a seismic source, which propagates outward in the form of dynamic load vibration waves. The distribution of seismic sources and propagation paths determines the distribution of the vibration field. Therefore, vibration not only acts as a triggering factor for coal burst but also represents the outcome of its occurrence, with released energy dissipating in the form of vibration energy, heat, and electromagnetic radiation. Among these, vibration energy can be monitored by various means, including microseismic, acoustic emission, and accelerometer sensors. Fig. 12 shows a research classification of elastic waves in rock masses based on frequency. In this experiment, the Polish SOS microseismic monitoring system and the American PCI-2 acoustic emission monitoring system were used to monitor the response characteristics of the vibration field under different mining intensities. The following analysis focuses on the results obtained from the acoustic emission monitoring system.

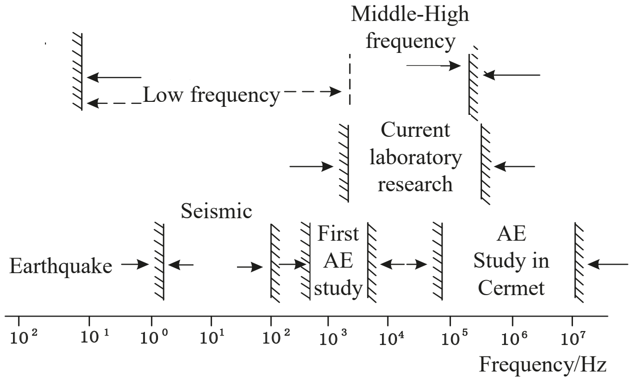

Fig. 12. Classification of elastic wave studies in rock mass by frequency

The absolute energy released by overburden fracturing under different mining intensities, as monitored by the PCI-2 acoustic emission system, is shown in Fig. 13.

As shown in Fig. 13(a), during mining at an extremely low intensity, the absolute energy monitored by the PCI-2 system exhibits significant low-level background noise signals. This indicates that the coal-rock mass underwent relatively sufficient micro-fracture development at this stage, and the energy release during the initial weighting was not prominent. Subsequently, the system effectively captured the energy released by the corresponding strata fracturing and movement during 7 periodic weightings, with peak values ranging between 1.0×10^6 aJ and 6.0×10^6 aJ. Absolute energy (in attojoules, aJ; 1 aJ = 10^{-18} J) was recorded. As shown in Fig. 13(b), under low-intensity mining, the low-level background signals in absolute energy decrease significantly. The initial weighting signal becomes more distinguishable, and the number of periodic weightings reduces to 5, with peak values ranging from 6.0×10^6 aJ to 1.0×10^7 aJ. This suggests that increased mining intensity leads to a higher energy level released by overburden fracturing. As shown in Fig. 13(c), under moderate-intensity mining, the energy release caused by the initial weighting becomes more pronounced, reaching a level of 2.0×10^7 aJ. This is followed by 4 periodic weightings, with energy peaks approximately in the range of 2.0×10^7 aJ to 3.0×10^7 aJ. This indicates that as mining intensity increases, the cantilever length gradually extends, the movement and evolution of the overburden become insufficient, and the caving blocks remain more intact. As shown in Fig. 13(d), under fast-intensity mining, the energy released during the initial weighting rapidly rises to 1.0×10^9 aJ. The subsequent periodic weightings further decrease to 4 times, with energy peaks approximately in the range of 2.0×10^9 aJ to 2.5×10^9 aJ. This demonstrates that high-intensity mining at this stage causes fracture of the high-position key stratum, thereby inducing higher-energy vibrations. As shown in Fig. 13(e), under extremely fast-intensity mining, low-level background signals are essentially absent. Both the initial and periodic weightings are very distinct, indicating that high-intensity mining is more likely to induce high-energy sudden events, corresponding to a higher risk of coal bursts.

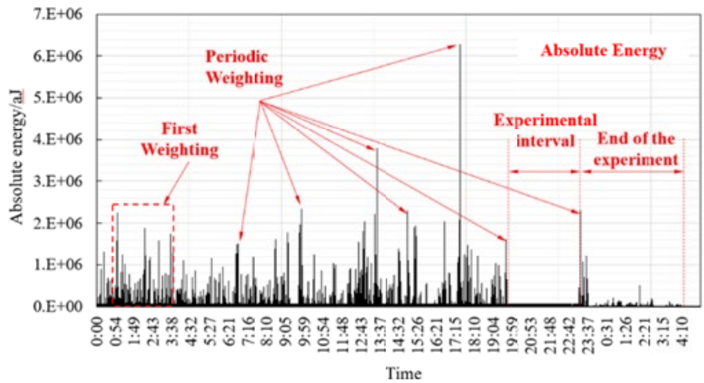

(a) Stage I

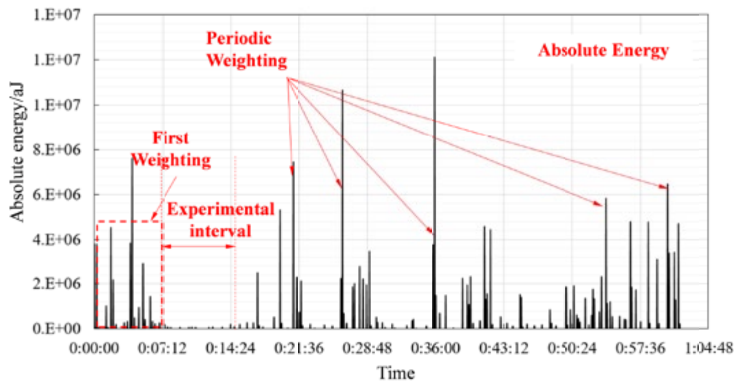

(b) Stage II

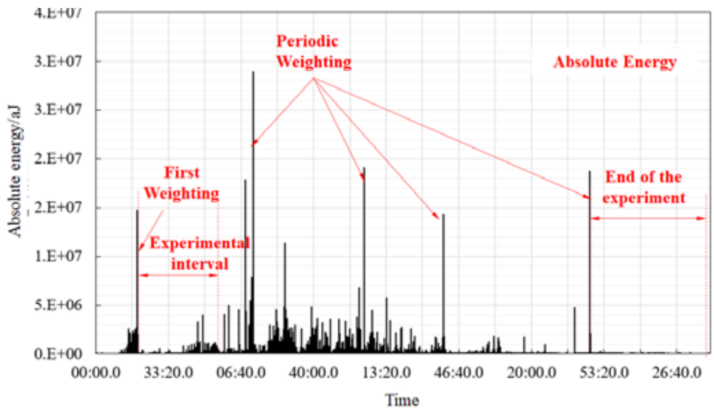

(c) Stage III

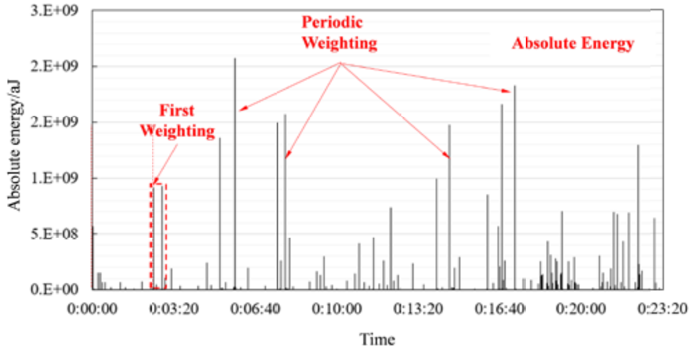

(d) Stage IV

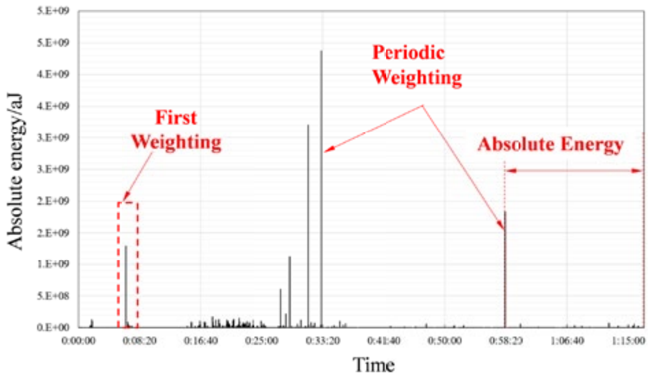

(e) Stage V

Fig. 13. Variation in Acoustic Emission absolute energy

As shown in Fig. 14, under different mining intensity conditions, the spatial distribution, energy release, and evolution patterns of acoustic emission (AE) seismic sources exhibit systematic differences, clearly reflecting the dynamic process of overburden fracturing from quantitative to qualitative change. During the extremely low-speed excavation stage, seismic sources are widely distributed in a “cloud-like” pattern near the excavation zone, characterised by a large number of low-energy events dominated by continuous micro-fracturing and particle friction. The rock mass has relatively sufficient time for stress adjustment, and the damage manifests as dispersed microscopic damage. As the mining intensity increases to the low-speed stage, seismic sources begin to cluster in the mid- to low-position overburden, showing an initial belt-like trend. Microcracks gradually propagate and connect; event frequency remains high, but energy increases slightly. Upon entering the moderate-speed excavation stage, seismic sources significantly migrate toward the mid- to high-position overburden, forming distinct concentration zones. Moderate- and higher-energy events increase, macroscopic cracks begin to penetrate, event frequency decreases while the energy released per event rises, marking the transition of overburden failure from discrete micro-fracturing to macroscopic fracturing. In the fast excavation stage, seismic sources become highly concentrated in the high-position overburden, especially along key stratum positions in a belt-like distribution. High-energy events dominate, and frequency further decreases, reflecting that the overburden has entered a rapid development phase of fracture zones, which can easily induce dynamic phenomena such as roof fracture and mine tremors. Under extremely fast excavation conditions, seismic sources are intensely concentrated in high-position or even roof areas, with spatial distribution approximating a concentrated fracture-plane pattern. This is accompanied by very few but extremely high-energy impact-type events, which indicates that when the mining advance rate is relatively high, i.e., when the excavation disturbance is relatively abrupt, the overburdened system does not have sufficient time to undergo slow and full movement and settlement. The stress field accumulates sharply and then suddenly releases, rapidly entering the next cycle. The failure mechanism of the overburden has shifted to systematic dynamic instability, significantly increasing the risk of coal burst and large-scale roof collapse.

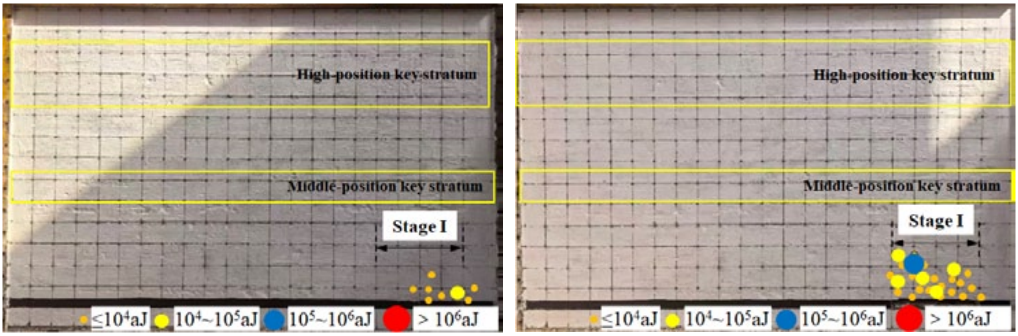

(a) Stage I

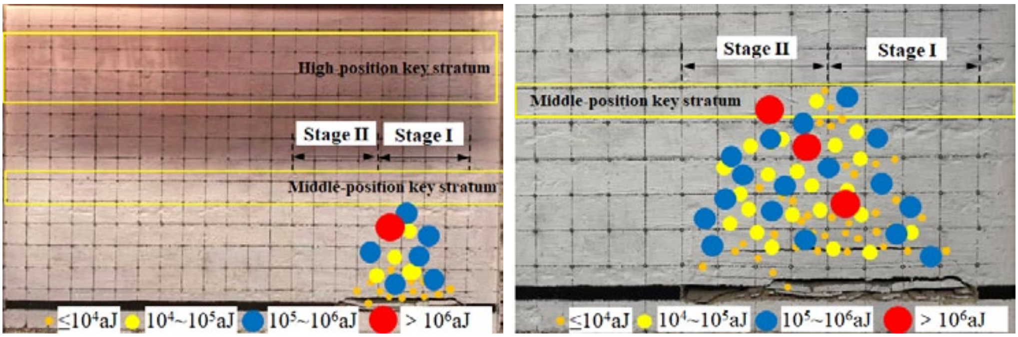

(b) Stage II

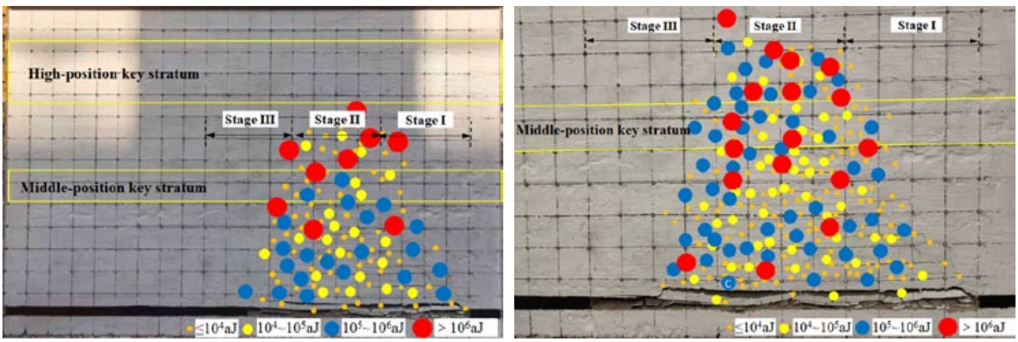

(c) Stage III

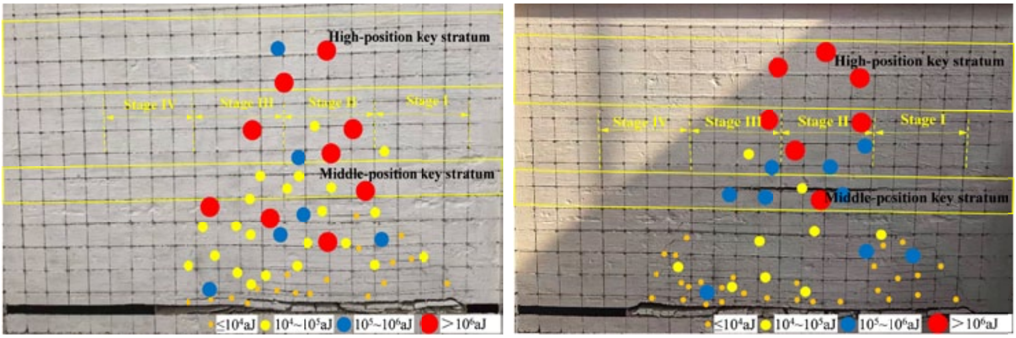

(d) Stage IV

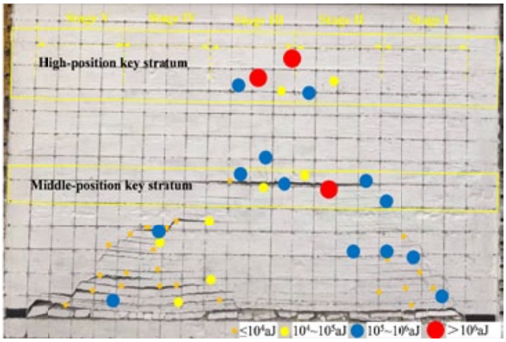

(e) Stage V

Fig. 14. Evolution of AE seismic sources under different mining intensities

Under low-speed mining conditions, the overburden is thoroughly fractured, and energy is released progressively, resulting in relatively dispersed seismic sources. In contrast, compared with normal mining speeds, high-intensity mining leads to severe failure of the overburden, with significant surface movement and deformation occurring over a short duration. Discontinuous deformation is more pronounced, with higher degrees of fracturing or step-like subsidence, primarily manifested as caving zones and water-conducting fracture zones. Creep failure is generally absent, and intense failure deformation occurs shortly after mining, resulting in sudden, large-scale fracturing. Under such conditions, the destructive potential of the overburden is greater, and high-energy events shift toward concentrated release in the upper strata.

In summary, as mining intensity increases, seismic sources evolve from widespread distribution to high-position concentration, and energy release shifts from dispersed to concentrated. Event frequency decreases while energy per event increases. This pattern provides clear guidance for strata control and disaster early warning.

3.4. Response characteristics of the intensity field

In the field of earthquake prediction, intensity is a crucial parameter for measuring the degree of building damage caused by earthquakes, playing a vital role in assessing potential seismic disasters and organising post-earthquake rescue efforts. The prediction of the intensity field relies fundamentally on accurate earthquake location. Drawing on relevant theories and techniques from seismology, this experiment employed a domestically produced BZ7201 high-precision accelerograph to monitor the response characteristics of the vibration field under different mining intensities.

As shown in Fig. 15(a), under extremely low-intensity mining conditions, the acceleration range is approximately ±0.6-0.8 m/s², exhibiting dense and continuous oscillations. Fluctuations are particularly pronounced within the interval of 0.05-0.25 seconds, with no distinct isolated spikes. This indicates that when the mining intensity is low, overburden fracturing resembles continuous friction or intensive micro-fracturing, making it difficult to isolate individual events. This reflects that the stress is in a stage of continuous adjustment to the secondary state of stress at this time.

Under relatively low-intensity mining conditions (Fig. 15b), the acceleration range is approximately ±0.8-1.0 m/s^2. The waveform exhibits distinct pulse-like spikes, indicating more pronounced suddenness. The stress concentration in the overburden increases, and the fracture mechanism gradually shifts from being dominated by particle friction and crack-friction slip to involving the coalescence of micro-cracks, the ejection of tiny rock fragments, or the local instability of micro-structures. Consequently, more pulse-characteristic vibration signals are generated.

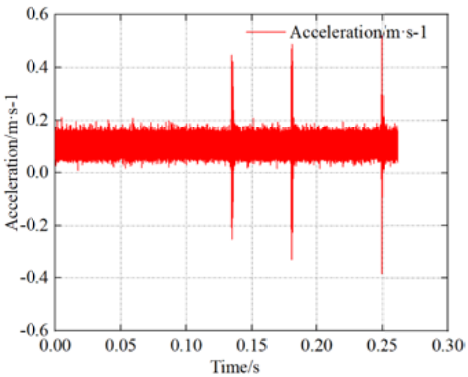

Typical signals 1

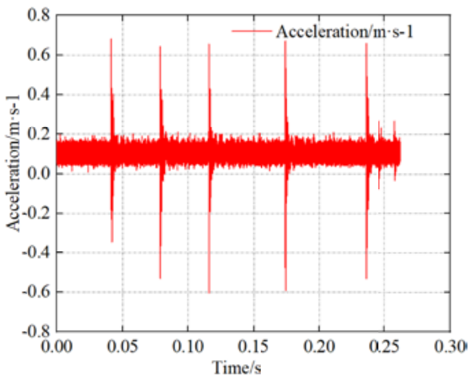

Typical signals 2

(a) Stage I

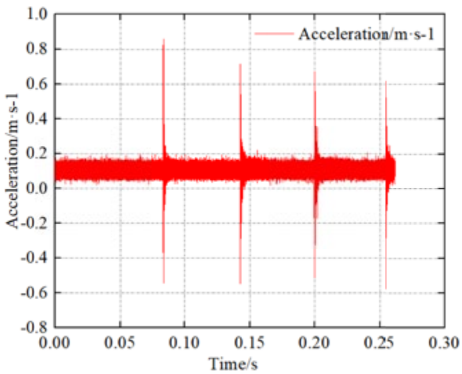

Typical signals 1

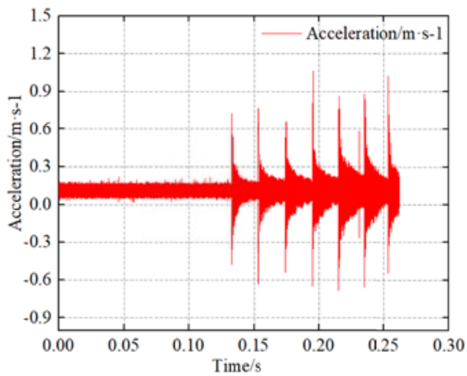

Typical signals 2

(b) Stage II

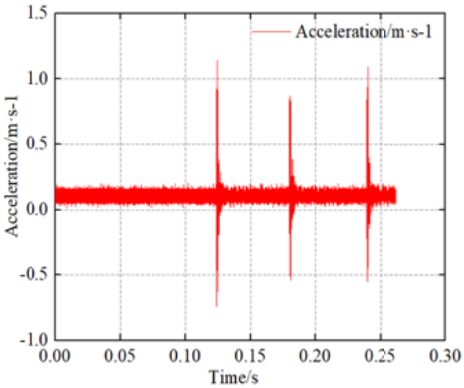

Typical signals 1

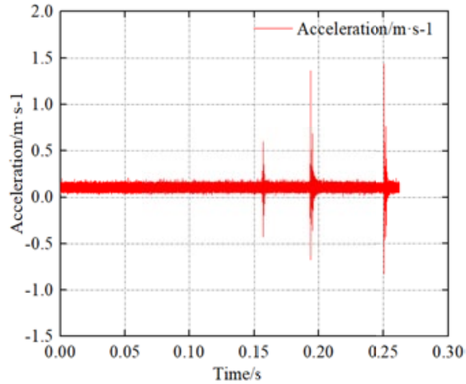

Typical signals 2

(c) Stage III

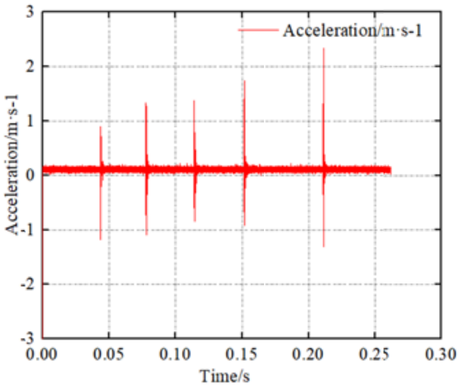

Typical signals 1

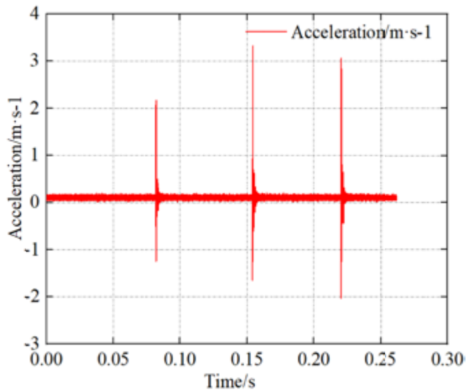

Typical signals 2

(d) Stage IV

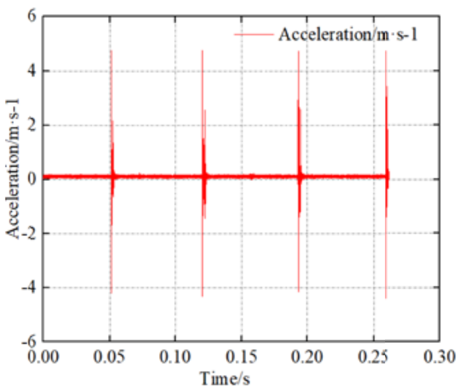

Typical signals 1

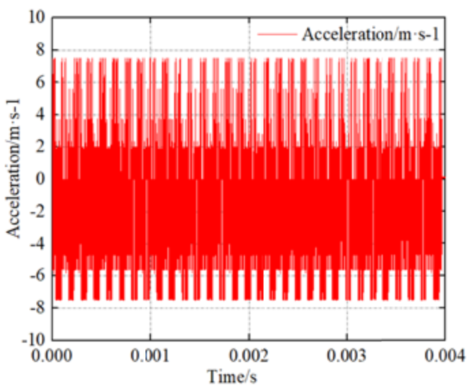

Typical signals 2

(e) Stage V

Fig. 15. Acceleration response characteristics under different mining intensities

Under moderate-intensity mining conditions (Fig. 15c), the acceleration range is approximately ±1.0-2.0 m/s^2. During this stage, the waveform exhibits sharp, isolated pulses, with relatively calm periods before and after each pulse. The pulse duration is shorter, indicating extremely high suddenness. The fracture scale has escalated from the microscopic level to the rapid propagation of macroscopic cracks or the instability of rock blocks, and the corresponding vibration modal frequency is lower. The spectrum completes the transition from "high-frequency dominance" to "low-frequency prominence."

As shown in Fig. 15(d), under fast-intensity mining conditions, the acceleration range is approximately ±3.0-4.0 m/s^2. The waveform morphology of the intensity field exhibits extremely sharp, high-amplitude isolated pulses or pulse pairs. Compared to lower or moderate mining intensities, the event frequency may decrease, but the energy and potential destructive force contained in individual events increase dramatically. Rapid mining causes the stress in the overburden to concentrate at an extremely high rate and exceed its overall strength limit. The fracture mechanism shifts to "impact-type" failure, such as instantaneous rupture of the key stratum, sudden large-scale roof subsidence, or induced mine tremors.

Under extremely fast-intensity mining conditions (Fig. 15e) the acceleration range is approximately ±6.0-10.0 m/s^2. The waveform exhibits a pronounced characteristic of strong impact-type vibration superimposed with oscillatory decay. This indicates that extremely fast mining causes the stress in the overburden to instantaneously far exceed the strength limit. The fracture mechanism is "explosive", corresponding to events such as large-scale instantaneous roof collapse, intense mine tremors, or coal burst.

Based on the systematic analysis of the overburden movement and intensity field response presented above, its evolution pattern emerges clearly: as the mining intensity increases, the signals evolve from continuous, low-amplitude oscillations through intermittent pulses to high-energy impact pulses, and finally, under extremely fast conditions, into giant pulses with extreme amplitudes and ultra-wide frequency bands. This progression reflects the qualitative transition in the fracture mechanism of the overburden – from the accumulation of microscopic damage, through the coalescence of macroscopic cracks, to the large-scale impact-type instability of rock masses. The stage-wise transitions in signal characteristics can serve as key criteria for grading the stability degradation of bedded rock mass over the longwall panel and for the early warning of coal burst risks. Identification of overstressed rock bed and its weakening can mitigate the acceleration rate of seismic signals and the number of mining tremors considerably [31].

4. Discussion

Based on the multi-field response characteristics of the stress field, seismic field, and intensity field, this study reveals the mining intensity effect of coal burst induced by the movement of composite key strata. Compared with existing research, this paper proposes that the structural transformation from a "voussoir beam" to a "cantilever beam" is the core manifestation of the mining intensity effect. It clarifies the differences in the timing and intensity of stress responses among high-level, medium-level, and low-level key strata, and constructs an evolutionary path of seismic signals from "continuous, low-energy, high-frequency" to "sudden, high-energy, low-frequency." The research conclusions have clear engineering application guidance for the source monitoring of overburden types.

4.1. Stress-energy mechanism considering the mining intensity effect

Overburden-type coal bursts are caused by the concentrated release of energy in coal and rock masses. Their primary source is the loading from overburden movement, although the failure location is often within the coal seam space. The elastic energy released by overburden fracturing and the gravitational potential energy applied to the coal body are the main energy sources for coal seam bursts. Coal extraction and unloading lead to the progressive dynamic adjustment of the stress and energy within the overburden structure of the stope. Upon reaching equilibrium, stress concentration zones and energy accumulation zones are formed. The higher the mining intensity, the greater the peak values of these stress concentrations and energy accumulation zones in the coal and rock strata. Furthermore, due to insufficient time for adjustment and transfer to deeper locations, these concentration zones are positioned closer to the free face of the coal wall.

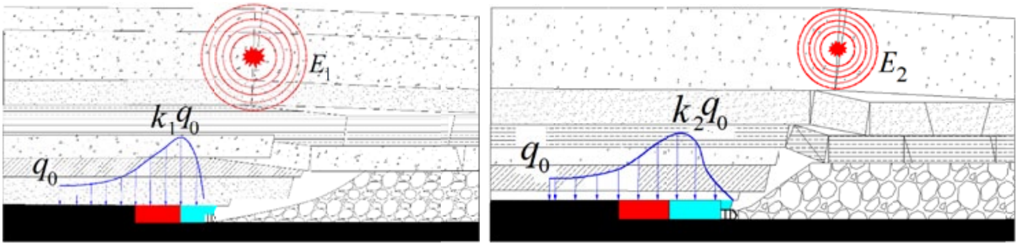

(a) High mining rate (b) Low mining rate

coal burst resistance zone, coal burst driving zone;

q_0 – Base stress, k_1, k_2 – Stress concentration factor of the coal mass under different mining intensities, E_1, E_2 – Roof-released energy under different mining intensities

Fig. 16. Schematic diagram of stope stress-energy release under different mining intensities

As illustrated in Fig. 16, the fractured zone and plastic zone in front of the coal wall constitute the coal burst resistance zone, while the area from the stress peak to the partially elevated stress section forms the coal burst driving zone. During high-speed mining, the widths of the fractured zone and plastic zone ahead of the coal wall decrease. Within a short period, the advance roof subsidence is relatively small, leading to an increase in the peak stress concentration factor and a sharp rise in energy released by roof fracturing. Consequently, the dynamic load from roof breakage, when superimposed on the high static load of the coal mass, can more readily breach the coal burst resistance zone and trigger a coal burst. Therefore, the mining intensity effect governs the stress and energy transfer process in overburden-type coal burst stopes.

4.2. Mechanism of overburden fracture and movement under high-intensity mining

Based on the aforementioned research and the overburden failure process associated with high-intensity mining, this paper proposes a mechanistic model for overburden movement-induced coal burst under high-intensity mining, as illustrated in Fig. 17. In the initial stage of working face retreat mining, the upper uncaved overburden behaves in the form of a thin plate, while the lower caved overburden forms a pressure arch. As the mining advance distance increases and the overburden continuously caves, the height and span of the "parallel pressure arch" increase accordingly. When the "pressure arch" has not yet reached its maximum height, the upper overburden continues to function as an "elastic thin plate" to maintain the stability of the overburden. Only when the height of the "pressure arch" reaches the bedrock surface does its span attain the maximum value, at which point the pressure arch undergoes periodic fracture, and the arch feet act upon the already caved rock, inducing stress concentration.

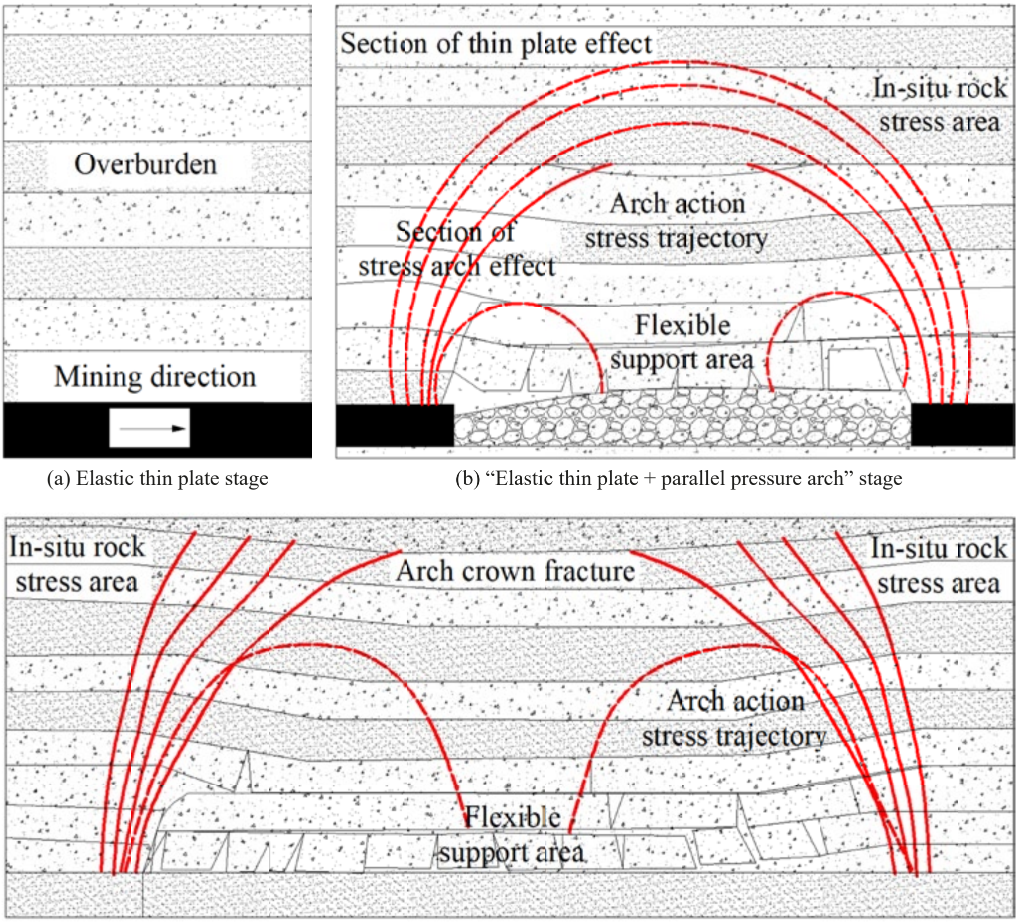

(a) Elastic thin plate stage

(b) "Elastic thin plate + parallel pressure arch" stage

(c) "Parallel pressure arch" and "elastic thin plate with a unilateral free edge" stage

Fig. 17. Mechanism model for overburden movement-induced coal burst under high-intensity mining

5. Conclusions

Regarding the mining intensity effect of coal burst induced by the movement of composite key strata, this study systematically investigated the differential characteristics of the displacement field, stress field, vibration field, and energy field in the high-, mid-, and low-position composite overburden under different mining intensities by combining physically similar material simulation with theoretical analysis. The main conclusions are as follows:

(1) After coal seam extraction, the composite key strata transition from layered bearing to synchronous bearing. As mining intensity increases, the cantilever length gradually extends, the activity of the overburden becomes increasingly insufficient, and the energy released by fracturing increases substantially, transforming the original low-position fractured voussoir beam structure (which had not yet contacted the goaf debris) into a high-position cantilever beam structure.

(2) As the advance rate increases, the ultimate suspended span of the overburden enlarges, resulting in intense dynamic load disturbance in the stope during periodic weighting and increasing the potential for instability of the overburden. Under high-speed mining conditions, the peak pressure-increase load is higher and located closer to the coal wall, causing the elastic core to be nearer to the exposed free surface, thereby greatly increasing the likelihood of coal burst occurrence.

(3) Under low-speed mining, the signals are dominated by low-energy events caused by continuous micro-fracturing and particle friction. As mining intensity increases, roof weighting becomes more pronounced, and seismic sources evolve from widespread distribution to concentration in high positions, while energy release shifts from dispersed to concentrated, indicating that high-intensity mining is more prone to inducing high-energy sudden events.

(4) When mining intensity is low, overburden fracturing resembles continuous friction or intensive micro-fracturing. As mining intensity increases, the signals evolve from continuous, low-amplitude oscillations (high-frequency dominance), through intermittent pulses (emergence of low-frequency components), to high-energy impact pulses (low-frequency dominance). This progression marks the qualitative transition in the fracture mechanism of the overburden – from the accumulation of microscopic damage, through the coalescence of macroscopic cracks, to large-scale impact-type instability of rock masses.

(5) When mining intensity is relatively low, the fracturing and movement of the overburden are relatively complete and stable, without significant roadway damage. Correspondingly, under high-speed mining in the field, the overburden exhibits large subsidence, intense fracturing and caving, and pronounced discontinuous deformation. Shear and tensile stress zones interact within the overburden, leading to significant dynamic failure in stress-concentrated areas, displaying characteristics of overburden-type coal burst damage. Therefore, based on the experimental conclusions, the reasonable and safe mining speed for this mine should be kept below 8.0 m/d whenever possible.

The research conclusions reveal the mining intensity effect of coal burst induced by the movement of composite key strata, which can help guide mines in determining reasonable mining intensities and in the source-level monitoring and early warning of coal burst hazard risks. It should be noted that the experimental conclusions of this study are based on the actual geological conditions of a specific mine and may have strong particularity. Subsequent research should be conducted under varying overburden characteristics, stope dimensions, mining techniques, and other conditions to further validate the applicability of the findings.

Acknowledgements

This research was carried out by the funded projects: Open Research Grant of Key Laboratory of Coal Mine Rock Burst Prevention & Control Technology and Equipment, National Mine Safety Administration (Grant ID SDEGIF-FC202501). Innovation Project of Shandong Energy Group. the Open Fund of the State Key Laboratory of Coal burst Theory and Prevention Technology National Mine Safety Administration (Preparatory) (Grant No. KFJJ-2025-0003). Basic Science (Natural Science) Research Projects in Higher Education Institutions of Jiangsu Province (Grant ID 25KJB440002). Open Research Project Funding from the National Key Laboratory of Coal Fine Exploration and Intelligent Development at China University of Mining and Technology (Grant ID SKLCRSM24KF019). The Taishan Industrial Experts Program (Grant ID tscx202408130).

References

[1] L.M. Dou, X.Y. Tian, A.Y. Cao, S.Y. Gong, H. H, J. H, W. C, X.W. Li, Present situation and problems of coal mine rock burst prevention and control in China. Journal of China Coal Society **47** (01), 152-171 (2022). DOI: http://doi.org/10.13225/j.cnki.jccs.yg21.1873

[2] Y.S. Pan, Y.M. Song, H. Luo, Y.H. Xiao, Coal bursts in China: theory, practice and management. Journal of Rock Mechanics and Geotechnical Engineering **16** (1), 1-25 (2024). DOI: http://doi.org/10.1016/j.jrmge.2023.11.003

[3] M.C. He, Q. Wang, Rock dynamics in deep mining. International Journal of Mining Science and Technology **33** (9), 1065-1082 (2023). DOI: http://doi.org/10.1016/j.ijmst.2023.07.006

[4] J.L. Xu, J.F. Ju, Structural morphology of key stratum and its influence on strata behaviors in fully-mechanized face with super-large mining height. Chinese Journal of Rock Mechanics and Engineering **30** (8), 1547-1556 (2011).

[5] Q.S. Li, Z.P. Ren, C. Zhang, J.Q. Ma, Y.Q. Zhao, X. He, P.H. Han, Characteristics of overburden-surface movement of high-intensity mining in Shangwan coal mine under the influence of advancing speed. Journal of Mining & Safety Engineering **41** (3), 437-449 (2022). DOI: http://doi.org/10.13545/j.cnki.jmse.2022.0459

[6] M.G. Qian, J.L. Xu, Behaviors of strata movement in coal mining. Journal of China Coal Society **44** (04), 973-984 (2019). DOI: http://doi.org/10.13225/j.cnki.jccs.2019.0337

[7] J.C. Wang, Z.H. Wang, Impact effect of dynamic load induced by roof in high-intensity mining face. Chinese Journal of Rock Mechanics and Engineering **34** (S2), 3987-3997 (2015). DOI: http://doi.org/10.13722/j.cnki.jrme.2014.1148

[8] S.L. Yang, Z.H. Wang, W. J, J.H. Y, Advancing rate effect on rock and coal failure format in high-intensity mining face. Journal of China Coal Society **41** (3), 586-594 (2015). DOI: http://doi.org/10.13225/j.cnki.jccs.2015.1944

[9] L.F. Feng, L.M. Dou, X.D. Wang, G.G. Xu, W. C, G.A. Zhu, B. J, Study on influence law of mining speed on stope energy releasing. Coal Science and Technology **48** (11), 77-84 (2020).

[10] Y.L. Yang, Y.X. Zhao, C. Zhang, J.Q. Ma, P.H. Han, Characterization method of overburden fracture damage in high-intensity mining based on energy dissipation. Journal of Mining & Safety Engineering **42** (01), 203-217 (2025). DOI: http://doi.org/10.13545/j.cnki.jmse.2022.0680

[11] C. Zhang, Z.P. Ren, S.Y. Lan, S.X. Fang, J.L. Lu, Y.D. Qiao, Quantitative characterization of coal mining damage and its application in numerical simulation. Journal of Mining Science and Technology **8** (3), 398-408 (2023). DOI: http://doi.org/10.19606/j.cnki.jmst.2023.03.013

[12] J.B. Liu, H.J. Zhang, G.C. Gao, W.T. Yan, J.D. Jing, Y. Li, Z.T, Ma, J.J. Chen, Analysis of overburden failure development height in high-intensity mining area in Western China. China Mining Magazine **33** (11), 121-129 (2024). DOI: http://doi.org/10.12075/j.issn.1004-4051.20240887

[13] Y. Li, T.H. Yang, H.L. Liu, X.G. Hou, H. Wang, Effect of mining rate on the working face with high-intensity mining based on microseismic monitoring: a case study. Journal of Geophysics and Engineering **14** (2), 350-358 (2017). DOI: http://doi.org/10.1088/1742-2140/aa5b5a

[14] W.B. Guo, G.B. Zhao, G.Z. Lou, S.R. Wang, Height of fractured zone inside overlying strata under high-intensity mining in China. International Journal of Mining Science and Technology **29** (1), 45-49 (2019). DOI: http://doi.org/10.1016/j.ijmst.2018.11.012.

[15] L.F. Feng, Q. Zhang, G.J. Liu, Influence mechanism of mining speed on energy release in a mine roof and elastic coal system. International Journal of Oil, Gas and Coal Technology **36** (2), 197-218 (2024). DOI: http://doi.org/10.1504/ijogct.2024.140286

[16] G.X. Xie, J.C. Chang, X.Z. Hua, Influence of mining velocity on mechanical characteristics of surrounding rock in fully mechanized top-coal caving face. Chinese Journal of Geotechnical Engineering **29** (7), 963-967 (2007).

[17] J.A. Wang, S.H. Jiao, X.G. Xie, Study on influence of mining rate on stress environment in surrounding rock of mechanized top-caving mining face. Chinese Journal of Rock Mechanics and Engineering **25** (5), 1118-1124 (2006).

[18] X.Z. Wang, J.L. Xu, W.B. Zhu, J.F. Ju, Influence of high mining velocity on periodic weighting during fully mechanized mining in a shallow seam. Journal of China University of Mining &. Technology **41** (3), 349-354 (2012).

[19] T.B. Zhang, W.Y. Guo, F. Guo, S.T. Gu, Analysis on energy accumulation and release of roof under influence of mining speed. Coal Science and Technology **46** (10), 37-44 (2018). DOI: http://doi.org/10.13199/j.cnki.cst.2018.10.006

[20] H.W. Zhang, Y.P. Li, Y. Chen, F. Zhu, L.F. Shao, Study on safety pushing forward speed of island coal mining face under hard roof and hard seam and hard floor conditions. Coal Science and Technology **45** (2), 6-11 (2017). DOI: http://doi.org/10.13199/j.cnki.cst.2017.02.002

[21] J.H. Liu, H. Sun, Z.J. Tian, F.X. Jiang, D. Li, Y. Wang, Q.J. Zhu, Effect of advance speed on rock burst in coal mines and its dynamic control method. Journal of China Coal Society **43** (7), 1858-1865 (2018). DOI: http://doi.org/10.13225/j.cnki.jccs.2017.1315

[22] Y.S. Pan, Q.X. Qi, F.X. Jiang, Interpretation of the Detailed Rules for the Prevention and Control of Coal Bursts in Coal Mines. China Coal Industry Publishing House. (2019).

[23] L.Z. Tang, J. Zhang, X.B. Li, L.H. Wang, J.X. Zhou, T. Liu, Research on response of mine microseismicity to mining rate based on quantitative seismology. Chinese Journal of Rock Mechanics and Engineering **31** (7), 1349-1354 (2012).

[24] J.H. Yang, X. W, Mechanical explanation of loading rate impact on tensile strength and its numerical simulation analysis. Journal of China Coal Society **42** (S1), 51-59 (2016). DOI: http://doi.org/10.13225/j.cnki.jccs.2016.1311

[25] Z.L. Li, X.Q. He, L.M. Dou, Control measures and practice for rock burst induced by overburden fracture in top-coal caving mining. Journal of China University of Mining &, Technology **47** (1), 162-171 (2018). DOI: http://doi.org/10.13247/j.cnki.jcumt.000799

[26] W.B. Guo, G.B. Zhao, E.H. Zhao, Critical failure of overlying rock strata and its criteria induced by high-intensity longwall mining. Journal of China Coal Society **45** (11), 3657-3666 (2020). DOI: http://doi.org/10.13225/j.cnki.jccs.2019.1335

[27] Z.X. Tan, Z.S. Wang, Y.J. Li, X.M. Sun, K.Z. Deng, Field research on ground subsidence rules of intensive fully-mechanized mining by sublevel caving. Journal of Mining & Safety Engineering **25** (1), 59-62 (2008).

[28] L.M. Fan, X.D. Ma, Y.H. Li, C. Li, W.C. Yao, M.X. Xiang, B.Y. Chu, J. Peng, Geological disasters and control technology in high intensity mining area of western China. Journal of China Coal Society **42** (2), 276-285 (2017). DOI: http://doi.org/10.13225/j.cnki.jccs.2016.6002

[29] J.L. Xu, W.B. Zhu, X.Z. Wang, Geological disasters and control technology in high intensity mining area of western China. Journal of China Coal Society **37** (05), 762-769 (2012). DOI: http://doi.org/10.13225/j.cnki.jccs.2016.6002

[30] J.Y. Guo, Q.S. Li, Surface damage characteristics in shallow-buried coal seam with strong disturbance mining: taking Shendong coal mine district as an example. China Mining Magazine **27** (4), 106-112 (2018).

[31] J.X. Zhuang, Z.L. Mu, X.F. Zhang, W. Cai, A.Y. Cao, C.L. Jiang, Małkowski, P. Seismic mitigation effect of overlying weakening strata in underground coal mines. Energies **16**, 5958 (2023). DOI: https://doi.org/10.3390/en16165958